Astron. Astrophys. 358, 708–716 (2000)

ASTRONOMY AND ASTROPHYSICS

Silicate emission in Orion⋆

D. Cesarsky[1,2], **A.P. Jones**[1], **J. Lequeux**[3], **and L. Verstraete**[1]

[1] Institut d'Astrophysique Spatiale, Bat. 121, Université Paris XI, 91405 Orsay CEDEX, France (ant@ias.fr; verstra@ias.fr)
[2] Max-Planck-Institut für Extraterrestrische Physik, 85741 Garching, Germany (diego.cesarsky@mpe.mpg.de)
[3] DEMIRM, Observatoire de Paris, 61 Avenue de l'Observatoire, 75014 Paris, France (james.lequeux@obspm.fr)

Received 7 December 1999 / Accepted 26 January 2000

Abstract. We present mid-infrared spectro-imagery and high-resolution spectroscopy of the Orion bar and of a region in the Orion nebula. These observations have been obtained in the Guaranteed Time with the Circular Variable Filters of the ISO camera (CAM-CVF) and with the Short Wavelength Spectrometer (SWS), on board the European Infrared Space Observatory (ISO). Our data shows emission from amorphous silicate grains from the entire H II region and around the isolated O9.5V star θ^2 Ori A. The observed spectra can be reproduced by a mixture of interstellar silicate and carbon grains heated by the radiation of the hot stars present in the region. Crystalline silicates are also observed in the Orion nebula and suspected around θ^2 Ori A. They are probably of interstellar origin. The ionization structure and the distribution of the carriers of the Aromatic Infrared Bands (AIBs) are briefly discussed on the basis of the ISO observations.

Key words: ISM: individual objects: Orion nebula – ISM: individual objects: Orion bar – stars: individual: θ^2 Ori A – ISM: H II regions – ISM: dust, extinction – infrared: ISM: lines and bands

1. Introduction

The Orion nebula is one of the most studied star-forming regions in the Galaxy. The ionizing stars of the Orion nebula (the Trapezium stars, the hottest of which is θ^1 Ori C, O6) have eroded a bowl-shaped H II region into the surface of the Orion molecular cloud. The Orion bar is the limb-brightened edge of this bowl where an ionization front is progressing into the molecular cloud. It is seen as an elongated structure at a position angle of approximately 60°. The Orion nebula extends to the North. The Trapezium stars are located at an angular distance of approximately 2.3 arc minutes from the bar, corresponding to 0.35 pc at a distance of 500 pc. The molecular cloud extends to the other side of the bar, but also to the back of the Orion nebula. The bright star θ^2 Ori A (O9.5Vpe) lies near the bar, and is clearly in front of the molecular cloud since its color excess is only E(B–V) $\simeq$ 0.2 mag.

Figs. 1 and 2 illustrate the geometry of the region observed. Fig. 1 shows six representative images of the region of the Orion bar (see the figure caption for details). Fig. 2 shows the contours of the the [Ne III] 15.5 μm fine-structure line emission which delineates the H II region. The emission in one of the mid-IR bands (hereafter called the Aromatic Infrared Bands, AIBs) at 6.2 μm traces the Orion bar (an edge-on PhotoDissociation Region or PDR). The AIBs are usually strongly emitted by PDRs. The Trapezium region was avoided because of possible detector saturation.

Pioneering infrared observations by Stein & Gillet (1969) and Ney et al. (1973) discovered interstellar silicate emission near 10 μm in the direction of the Trapezium. This was confirmed by Becklin et al. (1976) who also noticed extended silicate emission around θ^2 Ori A. Since that time, interstellar silicate emission has been found by the Infrared Space Observatory (ISO) in the H II region N 66 of the Small Magellanic Cloud (Contursi et al. in preparation) and in a few Galactic compact H II regions (Cox et al. in preparation) and Photodissociation Regions (PDRs, Jones et al. in preparation). The emission consists of two broad bands centered at 9.7 and 18 μm, which show little structure and are clearly dominated by amorphous silicates.

We report in the present article ISO observations of the Orion bar and of a part of the Orion nebula made with the Circular Variable Filter of the ISO camera (CAM-CVF) which allowed imaging spectrophotometry of a field $3' \times 3'$ at low wavelength resolution (R $\simeq$ 40). We also use an ISO Short-Wavelength Spectrometer (SWS) observation which provides higher-resolution ($R \simeq 1000$) spectroscopy at a position within the H II region (see Fig. 2). This spectrum was taken as part of the MPEWARM guaranteed-time program. We show here that these new ISO data confirm and extend previous observations of the amorphous silicate emission and also give evidence for emission by crystalline silicates.

Sect. 2 of this paper describes the observations and data reduction. In Sect. 3, we discuss the emission of dust and gas. The silicate emission is characterized in Sect. 4 through modelling of the observed continuum IR emission. Finally, conclusions are

Send offprint requests to: james.lequeux@obspm.fr

⋆ Based on observations with ISO, an ESA project with instruments funded by ESA member states (especially the PI countries: France, Germany, the Netherlands and the United Kingdom) and with the participation of ISAS and NASA.

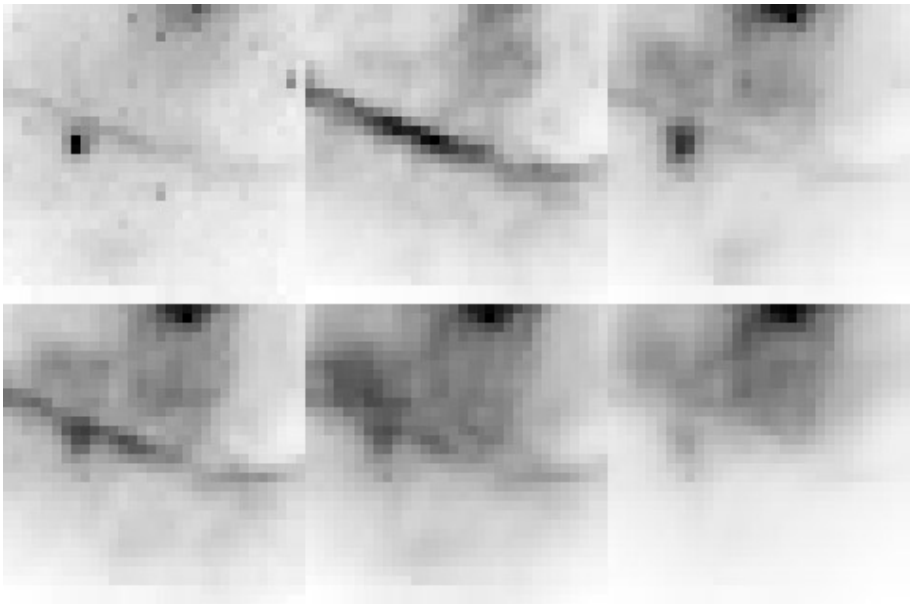

Fig. 1. Mosaic of six images of the Orion bar area (shown in detector coordinates, a clockwise rotation of 10.4° is needed to display the real sky orientation; see Fig. 2 for the equatorial coordinates). Top row: *(left)* an image at 5.01 μm, θ^2 Ori A is visible in the middle left of the image; *(centre)* the Orion bar at the AIB wavelength of 6.2 μm; *(right)* image at 9.5 μm(the wavelength of one of the silicate features), note that θ^2 Ori A is again visible. Bottom row: *(left)* image at the AIB wavelength of 11.3 μm and *(centre)* image at 12.7 μm (ISOCAM's CVF resolution blends [Ne II] and the 12.7 μm AIB feature); image at 15.6 μm*(right)*, wavelength of the [Ne III] forbidden line.

presented in Sect. 5. Our observations also give information on the fine-structure lines and on the AIBs. This will be presented in Appendices A and B respectively.

2. Observations and data reduction

Imaging spectrophotometry was performed with the 32×32 element mid-IR camera (CAM) on board the ISO satellite, using the Circular Variable Filters (CVFs) (see Cesarsky et al. 1996a for a complete description). The observations employed the 6″ per pixel field-of-view of CAM. Full scans of the two CVFs in the long-wave channel of the camera were performed with both increasing and decreasing wavelength. The results of these two scans are almost identical, showing that the transient response of the detector was only a minor problem for these observations. The total wavelength range covered is 5.15 to 16.5 μm and the wavelength resolution $\lambda/\Delta\lambda \simeq 40$. 10×0.28 s exposures were added for each step of the CVF, and 7 more at the first step in order to limit the effect of the transient response of the detectors. The total observing time was about 1 hour. The raw data were processed as described in Cesarsky et al. (1996b), with improvements described by Starck et al. (1998) using the CIA software[1]. The new transient correction described by Coulais & Abergel (1998) has been applied but the corrections introduced are minimal, as mentioned above. The bright star θ^2 Ori A is visible in the maps of several spectral components and has been used to re-position the data cube. This involved a shift of only 2″. The final positions are likely to be good to 3″ (half a pixel).

All the maps presented here were obtained from the CVF data cube and have approximately the same resolution: namely, 6″ pixels at the short wavelengths increasing to about 8″ at 15 μm; see Appendix C for more details.

[1] CIA is a joint development by the ESA Astrophysics Division and the ISOCAM Consortium led by the ISOCAM PI, C. Cesarsky, Direction des Sciences de la Matière, C.E.A., France

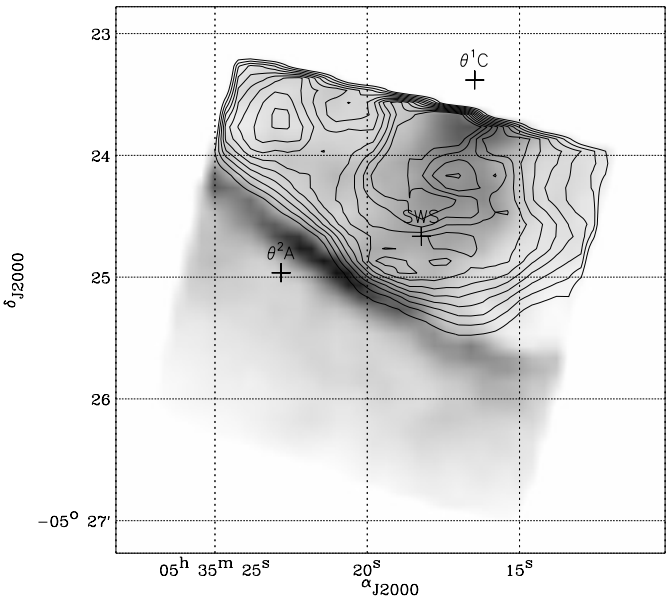

Fig. 2. [Ne III] map (contours) and 6.2 μm Aromatic Infrared Band (AIB) map (grey scale). The grey scale corresponds to line intensities from 0.01 to 0.30 erg s^{-1} cm^{-2} sr^{-1}. The contours correspond to band intensities of 0.015 to 0.06 erg s^{-1} cm^{-2} sr^{-1} by steps of 0.05. The cross is at the position of the O9.5V star θ^2 Ori A. The position of the hottest of the Trapezium stars (θ^1 Ori C) is also indicated, outside the observed field. The position of the SWS aperture in the direction of the H II region is shown by a black cross.

In several of these maps a faint emission can be seen on the south-east part of the ISOCAM field of view. This feature does not correspond to anything conspicuous in published images of the region, in particular in the near-IR images of Marconi et al. (1998). It is a spurious feature due to multiple reflections of the strong Trapezium between the detector and the CVF filter wheel, as shown by the ISOCAM ray tracing studies of Okumura (1999).

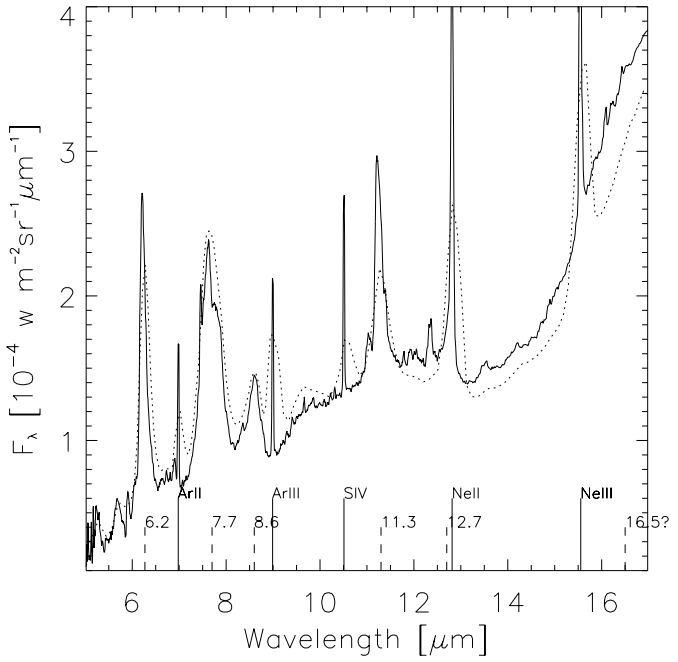

Fig. 3. The SWS spectrum (full line) compared to the CAM-CVF spectrum (dotted line). In this latter case, all the CAM pixels falling in the SWS aperture have been co-added.

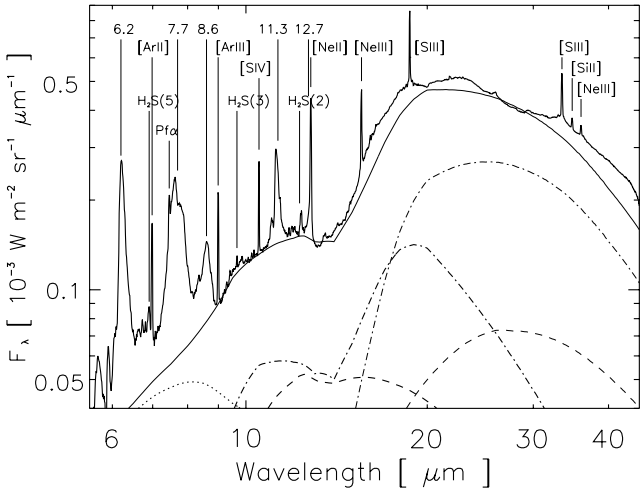

Fig. 4. SWS spectrum in the Orion nebula at the position shown in Fig. 2. A fit to the spectrum (see Sect. 3 for details) is shown which uses amorphous astronomical silicate (130 K: bold dashed-dotted, and 80 K: light dashed-dotted), amorphous carbon (155 K: bold dashed, and 85 K: light dashed), and amorphous carbon VSGs (300 K: dotted). The total calculated spectrum is given by the thin solid line. The identification of the strongest spectral features is indicated.

The complete SWS scan (2.4-46 μm) was reduced with the latest version of SWS-IA running at the Institut d'Astrophysique Spatiale. Calibration files version CAL-030 were used.

Fig. 3 presents the SWS spectrum ($\lambda/\Delta\lambda \simeq 1000$) obtained inside the H II region at the position indicated on Fig. 2. Fig. 3 also shows the comparison of the SWS spectrum with that of the CAM-CVF pixels averaged in the SWS aperture. The agreement between these spectra is excellent, well within 20 percent for the continuum.

3. Gas and dust emission

The spectra towards the H II region of the Orion nebula are shown in Figs. 3 and 4. The CAM-CVF spectrum of Fig. 3 is representative of the whole field because CVF spectra obtained at different positions in the H II region and around θ^2 Ori A look qualitatively similar (compare Figs. 3 and 10 which show the CVF spectra of different pixels; note particularly the rising long wavelength portion of the spectra).

In the SWS spectrum, a large number of unresolved lines from atoms, ions and molecules are visible. We note the Pfα recombination line of hydrogen (emitted by the warm, ionized gas of the H II region) and the molecular hydrogen pure rotation lines S(2) and very faintly S(3) and S(5) (stemming from the cooler, molecular PDR gas). The simultaneous presence of these lines reflects the variety of physical conditions present along the line of sight. Clearly, we are looking at emission from the H II region mixed with some emission from the background PDR. These unresolved lines are briefly discussed in Appendix A.

The other striking fact of the SWS spectrum is the strong continuum peaking at about 25 μm. It is emitted by warm dust in the H II region, but dust from the background PDR probably also contributes. The broad emission bands of amorphous silicates centered at 10 and 18 μm are visible. The classical AIBs at 6.2, 7.7, 8.6, 11.3 and 12.7 μm dominate the mid-IR part of the spectrum. As discussed by Boulanger et al. 1998, the mid-IR spectrum can be decomposed into Lorentz profiles (the AIBs) and an underlying polynomial continuum. Maps of the various AIBs constructed in this way all show the same morphology originating mainly from the PDR gas in the Orion bar (see Appendix B). We will hereafter use the 6.2 μm-band as representative of the behaviour of the AIBs.

In Fig. 5 we compare the behaviour of the mid-IR continuum emission and of the AIBs. Clearly, the AIB emission is concentrated in the Orion bar whereas the 15.5 μm-continuum emission extends throughout the whole CAM field and shows a local peak around θ^2 Ori A (note that the mid-IR emission around this star is foreground because the star lies in front of the nebula). The continuum emission, however, appears to peak towards θ^1 Ori C, outside the region observed with ISOCAM.

The contrast in the emission morphology between the bands and continuum can be interpreted in terms of the photodestruction of the AIB carriers in the hard UV-radiation field of the H II region. The AIB carriers must be efficiently destroyed while the larger grains are much more resistant (e.g. Allain et al. 1996). We detail the modelling of the dust thermal emission in the next section.

3.1. Modelling the dust emission

To account for the observed SWS spectra, we have calculated the thermal equilibrium temperature of dust in the Orion H II region

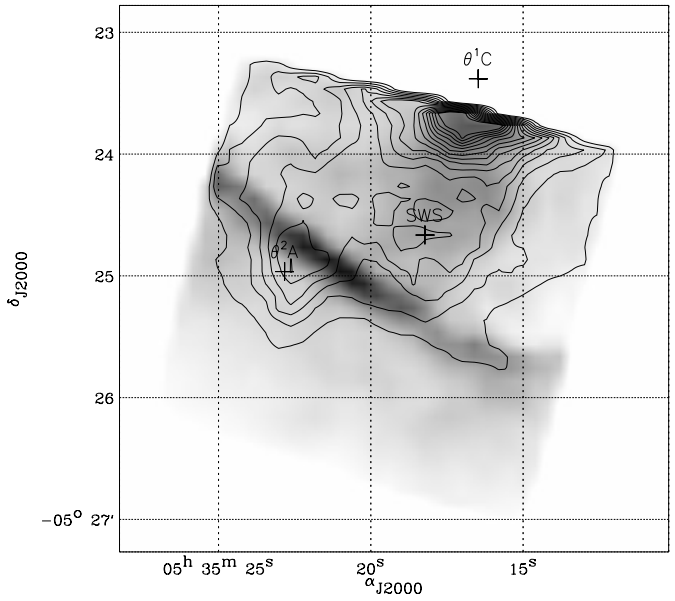

Fig. 5. Continuum emission at 15.5 μm (contours) superimposed on the AIB 6.2 μm map (grey scale). The continuum flux was taken to be the average of the flux on each side of the [Ne III]15.5 μm line. The 6.2 μm feature strength was estimated as explained in the Appendix C. The contours are from 10 to 80 Jy/pixel (1 pixel = $6'' \times 6''$), by steps of 5 Jy/pixel; the grey scale map spans 0.01 to 0.3 erg s^{-1} cm^{-2} sr^{-1}. The position of θ^2 Ori A is indicated by a cross.

as a function of distance of the Orion bar from the Trapezium stars, assuming that θ^1 Ori C (an O6 star) dominates the local radiation field. We use the optical constants of the amorphous astronomical silicate of Draine (1985) and of the amorphous carbon AC1 of Rouleau & Martin (1991). Assuming typical interstellar grain sizes (e.g. Draine & Lee 1984), we find a temperature range of 85–145 K for amorphous silicates and a range of 110–200 K for amorphous carbon, corresponding to grains of radius 1500 and 100 Å respectively, at a distance of ~ 0.35 pc from θ^1 Ori C (the distance of the Orion Bar to the Trapezium stars).

Using, for simplicity, discrete dust temperatures consistent with those calculated above ($T_{silicate}$ = 80 K and 130 K, T_{carbon} = 85 K and 155 K) we are able to satisfactorily model the continuum emission spectrum from the dust in the Orion H II region at the position of the ISO-SWS spectrum. In Fig. 4 we show the calculated emission spectrum from our model where we adopt the carbon/silicate dust mass ratios of Draine & Lee (1984). In the calculated spectrum we have included the emission from carbon grains at 300 K, containing $\sim$ 1 percent. of the total carbon dust mass, in order to fit the short wavelength continuum emission. The hot carbon grain emission mimics that of the stochastically-heated Very Small Grains (VSGs, Désert et al. 1990). The 300 K temperature represents a mean of the temperature fluctuations for these small particles in the radiation field of θ^1 Ori C, and therefore indicates a lower mass limit of $\sim$ 1 percent for the mass of the available carbon in VSGs.

The results of our model show that the emission feature in the 10 μm region is dominated by amorphous silicates at temperatures of the order of 130 K, but that there may also be a small contribution from amorphous carbon grains in the 12 μm region (Fig. 4). We also note broad "features" in the SWS spectrum, above the modelled continuum in Fig. 4, at $\sim 15-20$ μm, $\sim 20-28$ μm and longward of 32 μm, that are not explained by our model. These features bear a resemblance to the major bands at 19.5, 23.7 and 33.6 μm seen in the crystalline forsterite spectra of Koike et al. (1993) and of Jaeger et al. (1998). Bands in these same wavelength regions were noted by Jones et al. (1998) in the SWS spectra of the M 17 H II region and were linked with the possible existence of crystalline Mg-rich olivines in this object. Thus, similar broad emission bands are now observed in the 15–40 μm wavelength region of the SWS spectra of two H II regions (Orion and M 17). These bands resemble those of the crystalline Mg-rich silicate forsterite. Another band at 9.6 μm is probably due to some sort of crystalline silicate, and will be discussed in more details in the next section.

This dust model is simple-minded but emphasizes dust spectral signatures in the mid-IR continuum which was the main aim here. More detailed modelling treating temperature fluctuations and taking into account the grain size distribution is underway (Jones et al. in preparation).

The broad continua that lie above the model fit (i.e. $\sim 20-28$ μm and > 32 μm, Fig. 4) can be associated with crystalline silicate emission bands. This seems to be a robust conclusion of this study. The features are too narrow to be explained by single-temperature blackbody emission and are therefore likely to be due to blended emission features from different materials. Unfortunately, having only one full SWS spectrum and CVF spectra that do not extend beyong 18 μm, we are unable to say anything about the spatial variation of these broad bands in the Orion region.

Interestingly, broad plateaux in the $\sim 15-20$ μm region have been associated with large aromatic hydrocarbon species containing of the order of a thousand carbon atoms (van Kerckhoven et al. 2000). However, in this study the integrated intensity of the $\sim 15-20$ μm plateaux do vary by a factor of up to 10 relative to the aromatic carbon features shortward of 13 μm. Thus, the origin of these broad emission features does remain something of an open question at this time.

4. Tracing the silicate emission

To delineate the spatial extent of the 10 μm-silicate emission conspicuously visible in Figs. 3 and 4, we proceed as follows. We start with the spectrum towards θ^2 Ori A, which shows the most conspicuous silicate emission and we represent the AIBs by Lorentz profiles, see Fig. 6 (top). Next we subtract them from the CVF spectra. The remaining continuum has the generic shape of a blackbody on top of which we see the broad bands corresponding to the silicate emission, Fig. 6 (middle). Finally, we subtract a second order polynomial from the continuum thus obtaining the well known silicate emission profile at that position, Fig. 6 (bottom). The profile thus obtained is then used as a scalable template to estimate the emission elsewhere, see Appendix C for more details.

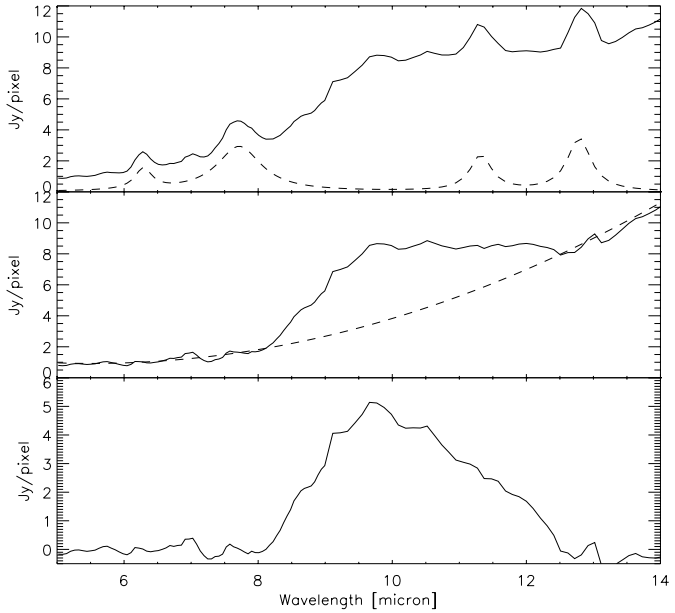

Fig. 6. *Top panel:* CVF spectrum towards θ^2 Ori A (solid line). The ordinates give fluxes in Jy per $6'' \times 6''$ pixel. A Lorentz fit to the AIBs is shown as the dotted line. *Middle panel:* result of the subtraction of the AIBs from the CVF spectrum. The fit to the continuum is shown by the dotted line. *Bottom panel:* Residual from the middle figure, i.e. the suspected amorphous silicate emission profile; notice the narrower bump near 9.6 μm.

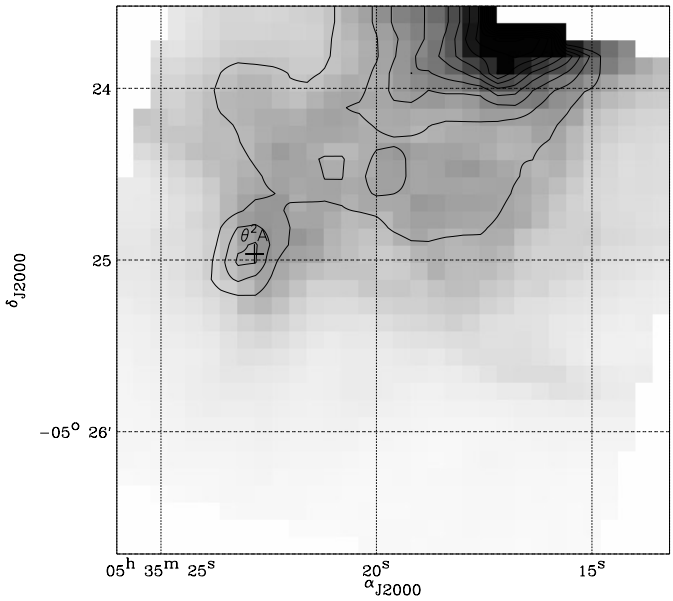

Fig. 7. Map of the intensity of the broad 9.7 μm band of amorphous silicates (contours) superimposed on the 15.5 μm continuum map (grey scale). Note the bright silicate emission around θ^2 Ori A (cross). The contours correspond to integrated band intensities from 0.25 to 0.7 erg s^{-1} cm^{-2} sr^{-1} by steps of 0.05; the gray image spans from 1 to 80 Jy/pixel.

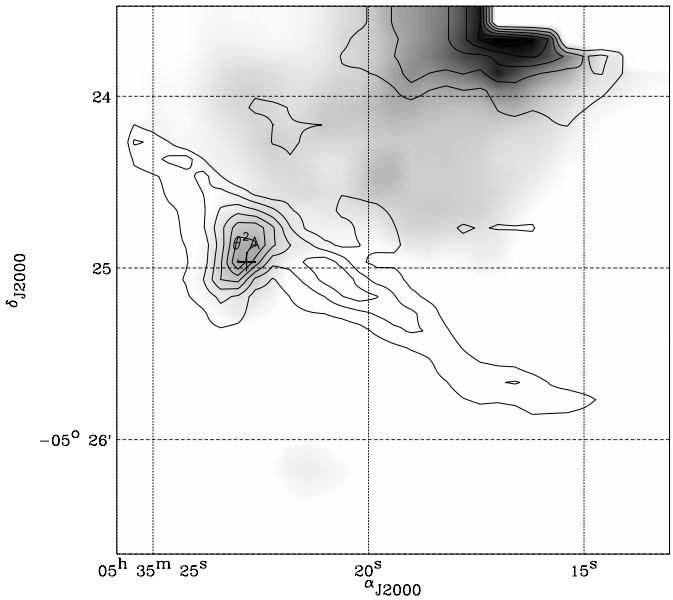

Fig. 8. Map of the 9.6 micron feature map (contours) superimposed on the map of the broad 9.7 μm band of amorphous silicates (grey scale spanning 0.1 to 10 erg s^{-1} cm^{-2} sr^{-1}. The contours correspond to integrated band intensities from 0.02 to 0.11 erg s^{-1} cm^{-2} sr^{-1} by steps of 0.001. The shift with respect to the position of θ^2 Ori A (cross) is by less than one pixel and may not be significant.

On top of the broad band of amorphous silicate centered near 9.7 μm we see a band centered at nearly 9.6 μm, which we ascribe to crystalline silicates (Jaeger et al. 1998). This band was also used as a scalable template as explained above and in Appendix C. Finally, the S(5) rotation line of H_2 at 6.91 μm is present and is probably blended with the [Ar II] line at 6.99 μm.

In Fig. 7, we see that the spatial distribution of the 9.7 μm-feature of amorphous silicate is quite similar to that of the 15.5 μm-continuum. The 15.5 μm continuum emission includes a strong contribution from silicates (see Fig. 4), but a peak in the silicate emission around θ^2 Ori A is also evident. The silicate emission is thus predominantly due to larger grains. The narrower 9.6 μm feature is mapped in Fig. 8. We note its similarity to the distribution of the 9.7 μm broad band: this fact lends support to our assignation of this band to crystalline silicate.

Due to the low spectral resolution of the CAM-CVF, however, the 9.6 μm feature will certainly blend with the S(3) pure rotational line of molecular hydrogen - if present. To check this we have compared our 9.6 μm map to that of molecular hydrogen in its fluorescent vibrational line $1 \rightarrow 0$ S(1) (2.12 μm). Courtesy of P.P. van der Werf (van der Werf et al. 1996), we reproduce in Fig. 9 the map of the fluorescent molecular hydrogen emission. This latter correlates better with the AIB emission as traced by the 6.2 μm-feature (bottom figure) than it does with the tentative crystalline silicate emission (top), namely they both peak along the bar. This is not surprising because the H_2 and AIB emitters require shielding from far-UV radiation to survive. Conversely, the 9.6 μm silicate feature is stronger where H_2 is weak as can be seen around θ^2 Ori A. In addition, the H_2 S(3) rotational line at 9.66 μm is detected in the ISO-SWS spectrum of the Orion bar presented in Verstraete et al. (1999, in preparation) with an intensity of 6×10^{-7} W m^{-2} sr^{-1}. This value

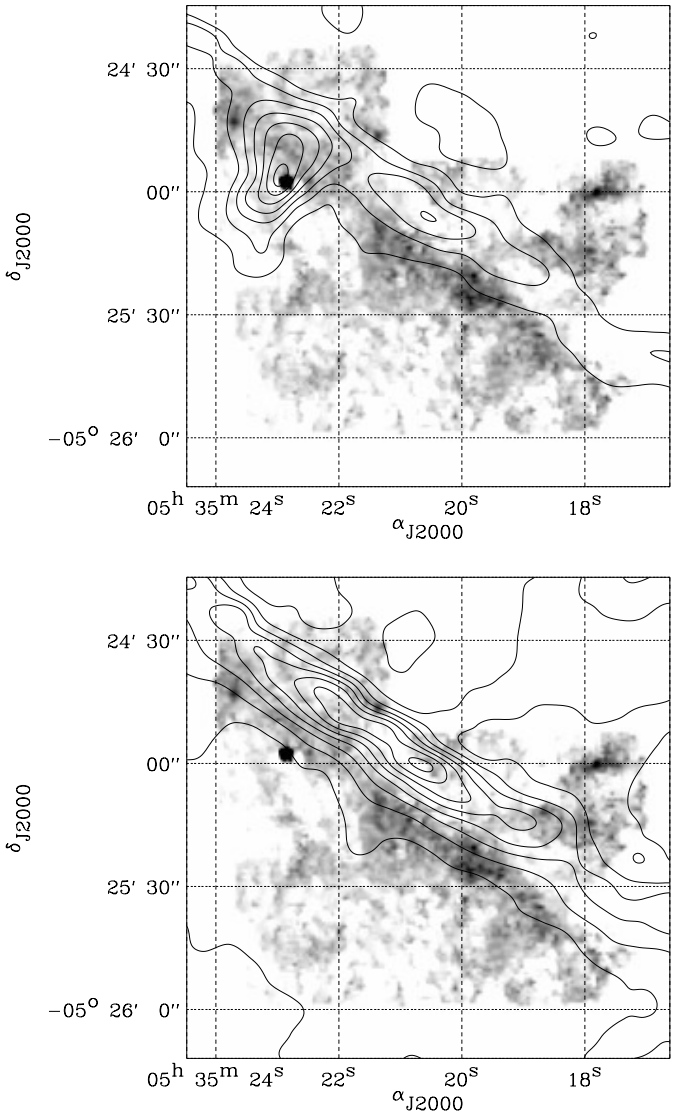

Fig. 9. The 9.6 μm feature (top) and 6.2 μm-AIB (bottom) both in contours superimposed to the $v = 1 \rightarrow 0$ S(1) line emission of molecular hydrogen taken from van der Werf et al. (1996) (grey scale). The contours correspond to integrated band intensities from 0.02 to 0.11 by steps of 0.01 (top figure) and 0.045 to 0.27 by steps of 0.025 (bottom figure) in units of erg s^{-1} cm^{-2} sr^{-1}.

is a factor of 16 below the median flux of the 9.6 μm feature in our map, namely 10^{-5} W m^{-2} sr^{-1}. We can thus safely conclude that our 9.6 μm-emission predominantly originate from silicates. A confirmation of the identification of the 9.6 μm band with a crystalline silicate dust component would be possible if a second signature band were seen in our spectra. The SWS spectrum (Fig. 4) shows only broad emission bands that are difficult to characterise, snd additionally, the chacteristic crystalline olivine band in the $11.2 - 11.4$ μm region (e.g. Jaeger et al. 1998), if present, is blended with the 11.2 μm aromatic hydrocarbon feature. Additionally, most of the chacteristic crystalline bands fall longward of the CVF spectra. Thus, it is difficult to self-consistently confirm the 9.6 μm band identification with the presented data.

In summary, emission in the 9.7 μm band of amorphous silicate emission exists everywhere inside the Orion H II region. Previously, amorphous silicate emission had only been seen in the direction of the Trapezium (Stein & Gillett 1969; Forrest et al. 1975; Gehrz et al. 1975). We may assume that the 18 μm band is also widely present in the region, as witnessed by the single SWS spectrum (Fig. 4) and by the generally rising long wavelength end of ISOCAM spectra; the two spectra shown, Figs. 3 and 10 are quite representative of the steeply rising continuum longward of 15 μm.

4.1. The interstellar silicate and H_2 emission around θ^2 Ori A

The case of θ^2 Ori A is particularly interesting because the geometry is simple and therefore allows quantitative calculations. Moreover, the thermal radio continuum, the recombination lines and the fine-structure lines are faint in the neighbourhood of this star (Felli et al. 1993; Pogge et al. 1992; Marconi et al. 1998, and the present paper, Fig. 2). θ^2 Ori A is classified as an O9.5Vpe star and shows emission lines (see e.g. Weaver & Torres-Dodgen 1997). It is a spectroscopic binary and an X-ray source. There is little gas left around the star and the observed silicate dust (Fig. 8) is almost all that is visible of the interstellar material left over after its formation. Indeed, O stars are not known to produce dust in their winds which are probably much too hot, so that the silicates we see here must be of interstellar origin.

The mid-IR continuum observed towards θ^2 Ori A can be accounted for by combining emission of warm silicate and carbon grains (see Fig. 10). The model continuum was obtained in the same way as for the SWS observation (see Fig. 4) and with the same assumptions. The grain temperatures are consistent with the heating of interstellar grains by the strong radiation field of the star.

As discussed above, the band near 9.6 μm (Fig. 6 bottom and Fig. 8) may be due to crystalline silicates, any contribution of the S(3) H_2 line to this band is minor. Another band at 14 μm (see Figs. 4 and 10) might also be due to crystalline silicates. Amongst the crystalline silicates whose mid-IR absorption spectra are shown by Jaeger et al. (1998), synthetic enstatite (a form of pyroxene) might perhaps match the θ^2 Ori A spectrum. The interest in the possible presence of crystalline silicates around this star is that they would almost certainly be of interstellar origin, pre-dating the formation of the star. Observations at longer wavelengths are needed for a definitive check of the existence of crystalline silicates and for confirming their nature. Such observations do not exist in the ISO archives and should be obtained by a future space telescope facility.

5. Conclusions

We obtained a rather complete view of the infrared emission of the Orion nebula and its interface with the adjacent molecular cloud. The most interesting results are the observation of amorphous, and possibly crystalline, silicates in emission over

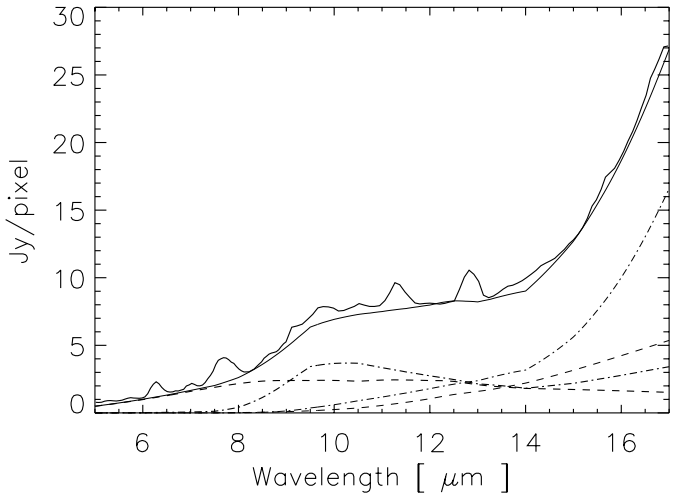

Fig. 10. CVF spectrum towards θ^2 Ori A (heavy solid line). The ordinates give fluxes in Jy per $6'' \times 6''$ pixel. The fit to the continuum is shown by the thin solid line. The fit (see Sect. 3) to these data comprises, from top to bottom on the right-hand axis: 100-K amorphous astronomical silicate (dot-dashed line), 110-K amorphous carbon (dashed line), 235-K amorphous astronomical silicate (dot-dashed line) and 330-K amorphous carbon emission (dashed line).

the entire H II region and in an extended region around the bright O9.5Vpe star θ^2 Ori A. We have fitted the mid-IR continuum of the H II region and around θ^2 Ori A with the emission from amorphous silicate and amorphous carbon grains at the equilibrium temperatures predicted for the grains in the given radiation field. This shows that both types of grains can survive in the harsh conditions of the H II region. A number of bands (the 9.6 μm bump seen in Fig. 6; the excess 14 μm emission indicated in Figs. 4 and 10) suggest emission from crystalline silicates (essentially forsterite) in the H II region. Crystalline silicates may also exist around θ^2 Ori A, but further, longer wavelength observations are required to confirm their presence.

Do the observed crystalline silicates result from processing of amorphous silicates in the H II region or in the environment of θ^2 Ori A? Silicate annealing into a crystalline form requires temperatures of the order of 1000 K for extended periods (Hallenbeck et al. 1998). The dust temperatures observed in the H II region and around θ^2 Ori A are considerably lower than this annealing temperature. One might however invoke grain heating following grain-grain collisions in the shock waves that are likely to be present in the H II region. However, grain fragmentation rather than melting is the more likely outcome of such collisions (Jones et al. 1996). It is probable that the crystalline silicates observed here were already present in the parent molecular cloud, and probably originate from oxygen-rich red giants.

Emission by both amorphous and crystalline silicates has been observed with ISO around evolved stars (Waters et al. 1996; Voors et al. 1998). The crystalline silicates there must have been produced locally by annealing of amorphous silicates. Gail & Sedlmayr (1999) have shown that this is possible, and that both amorphous and crystalline forms can be released into the interstellar medium. However, there is no evidence for absorption by crystalline silicates in the general interstellar medium in front of the deeply embedded objects for which amorphous silicate absorption is very strong (Demyk et al. 1999; Dartois et al. 1998). Consequently, crystalline silicates represent only a minor fraction compared to amorphous silicates. It would be difficult to detect the emission from a small crystalline component of dust in the diffuse interstellar medium because the dust is too cool ($T \sim 20$ K) to emit strongly in the $15 - 40\,\mu$m wavelength region. Observations of H II regions and bright stars provide the opportunity of observing this emission due to the strong heating of dust. Emission from amorphous and crystalline silicates is seen around young stars (Waelkens et al. 1996; Malfait et al. 1998) as well as in comets (Crovisier et al. 1998). There are also silicates in meteorites, but their origin is difficult to determine because of secondary processing in the solar system. Crystalline silicates in comets, and perhaps in interplanetary dust particles believed to come from comets (Bradley et al. 1992), must be interstellar since the material in comets never reached high temperatures. However, the silicates probably experienced changes during their time in the interstellar medium. It is interesting to note that while very small grains of carbonaceous material exist, there seem to be no very small silicate grains in the interstellar medium (Désert et al. 1986).

Acknowledgements. A.P. Jones is grateful to the Société de Secours des Amis des Sciences for funding during the course of this work. We are grateful to P.P. van der Werf for providing us with his map of molecular hydrogen emission.

Appendix A: the mid-IR line emission from the Orion nebula

We presented in Fig. 2 a map of the studied region in the [Ne III] line at 15.5 μm. Fig. A.1 displays the map of the [Ar II] line at 7.0 μm superimposed on the map of the [Ar III] 9.0μm line. These maps illustrate the ionization structure of the Orion nebula. The spectral resolution of the CVF does not allow a separation of the the [Ar II] line at 6.99 μm from the S(5) pure rotation line of H_2 at 6.91 μm. However, the bulk of the H_2 emission come from deeper in the molecular cloud than that of [Ar II], *ie.* more to the south-west (see Fig. 9) and the contamination by the S(5) line is probably minor. The SWS spectrum shown here and that taken towards the bar (Verstraete et al. 1999, in preparation) in which the [Ar II] and the H_2 S(5) line are well separated from each other, show that the H_2 line is a factor 4 or 5 weaker and hence cannot seriously contaminate the [Ar II] map.

The emission by the singly-charged ion [Ar II] is concentrated near the ionization front on the inner side of the bar. This is very similar to what is seen in the visible lines of [N II] λ6578 and [S II] λ6731 (Pogge et al. 1992 Fig. 1c and 1d). The detailed correspondence between the maps in these three ions is excellent: note that the optical maps are not much affected by extinction. The ionization potentials for the formation of these ions are 15.8, 14.5 and 10.4 eV for Ar II, N II, S II respectively, and are thus not too different from each other.

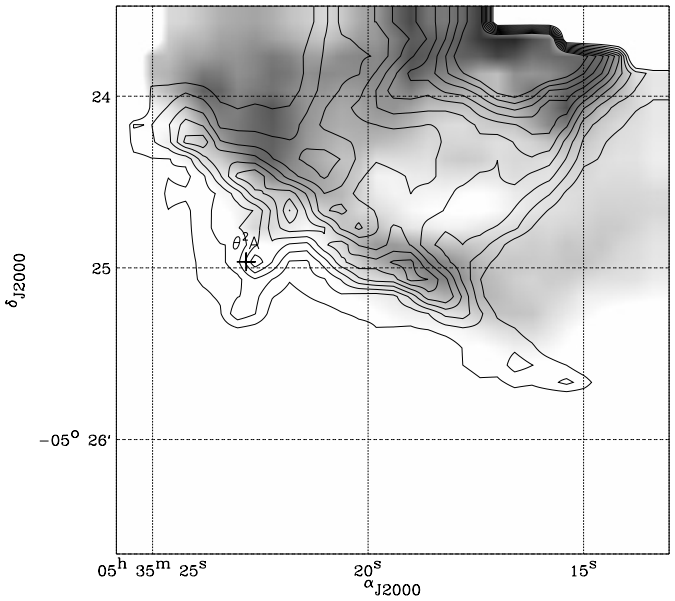

Fig. A.1. Map in the line of [Ar II] at 7.0 μm (contours) superimposed on the map of the [Ar III] 9.0 μm line (grey scale spanning 0.01 to 0.05 erg s^{-1} cm^{-2} sr^{-1}). The contours for [ArII] are from 10^{-3} to 10^{-2} erg s^{-1} cm^{-2} sr^{-1} by steps of 10^{-3}. The position of θ^2 Ori A is indicated by a cross. The peak at 7 μm at this position is probably due to the S(5) line of H_2 rather than to [Ar II] (see text).

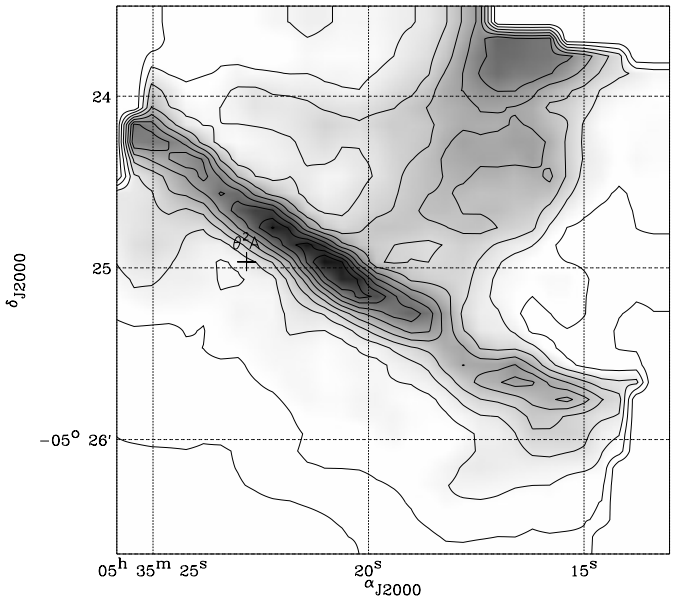

Fig. B.1. Map of the 11.3 μmUIB (contours) superimposed on the 6.2 μmUIB map (grey scale from 0.05 to 0.3 erg s^{-1} cm^{-2} sr^{-1}). The contours correspond to integrated band intensities from 0.016 to 0.16 erg s^{-1} cm^{-2} sr^{-1} by steps of 0.016. The distributions of the two UIBs are extremely similar. The position of θ^2 Ori A is indicated by a cross.

The emission from the doubly-charged ions [Ne III] and [Ar III] shows a very different spatial distribution, with little concentration near the bar but increasing towards the Trapezium. The [Ne III] map (Fig. 2) is very similar to the [O III]λ5007 line map (Pogge et al. 1992 Fig. 1*e*), as expected from the similarity of the ionization potentials of [Ne II] and [O II], respectively 41.1 and 35.1 eV. However, the distribution of the [Ar III] line (Fig. A.1) is somewhat different, with a trough where the [Ne III] and the [O III] lines exhibit maxima. Ar III is ionized to Ar IV at 40.9 eV, almost the same ionization potential as that of Ne II, so that Ar IV (not observable) should co-exist with Ne III and Ar III with Ne II. A map (not displayed) in the 12.7 μm feature, which is a blend of the 12.7 μm AIB and of the [Ne II] line at 12.8 μm, is indeed qualitatively similar to the [Ar III] line map in the H II region. It differs in this region from the maps in the other AIBs, showing that it is dominated by the [Ne II] line.

As expected, the dereddened distribution of the Hα line (Pogge et al. 1992 Fig. 3*b*), an indicator of density, is intermediate between that of the singly-ionized and doubly-ionized lines.

Appendix B: the AIB emission

Maps of the emission of the 6.2 and 11.3μm AIBs are shown in Fig. B.1. We do not display the distribution of the other AIBs because they are very similar. All the spectra of Figs. 3, 4 and 6 show the classical UIBs at 6.2, 7.7, 8.6, 11.3 and 12.7 μm (in the CAM-CVF data the latter is blended with the [Ne II] line at 12.8 μm). There are fainter bands at 5.2, 5.6, 11.0,, 13.5 and 14.2 μmvisible in the SWS spectrum of Fig. 3: they may be AIBs as well. All the main bands visible in the CVF spectra are strongly concentrated near the bar. Emission is observed everywhere, because of the extension of the PDR behind the Orion nebula and the presence of fainter interfaces to the South-East of the bar. We confirm the general similarity between the distributions of the different AIBs through the Orion bar observed by Bregman et al. (1989).

We thus conclude that, although the excitation conditions vary greatly from the Trapezium region towards the South-West of the bar, the mixing of fore- and background material along the line of sight does not allow us to observe spectroscopical changes in the AIB emission features (due e.g. to ionization or dehydrogenation as in M17-SW, Verstraete et al. 1996).

Appendix C: estimates of emission strengths

Spectral emission maps have been obtained using one or another of three different methods. The emission from well defined and rather narrow spectral features, viz. AIBs and ions, can be estimated either by numerical integration of the energy within the line and an ad-hoc baseline (*method 1*), or by simultaneous fit of Lorentz (Boulanger et al. , 1998) and/or gauss profiles, including a baseline, determined by a least square fitting algorithm (*method 2*). The strength of features not amenable to an analytical expression, like the suspected amorphous silicate emission (see Fig. 6) has been estimated using the following method (*method 3*). We have constructed an emission template consisting of all the observed emission features, each one arbitrarily normalised to unit peak intensity, see Fig. C.1. A least square computer code was then used to obtain, for each of the 32×32 lines of sight, a set of multiplying coefficients for each

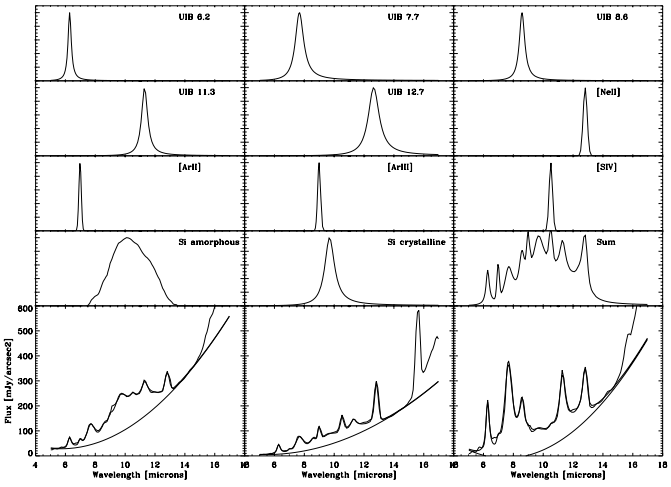

Fig. C.1. The eleven line and band templates, normalized to unit peak intensity, used by the least square fitting code (first eleven panels; the 12th panel, labeled Sum, shows the combined template). The low three panels give examples of the fit goodness for three lines of sight (from left to right): towards θ^2 Ori A; towards a "hot spot" in the H II region; and towards a "hot spot" on the AIB emission. For all lines of sight the fit was stopped at 15 μm since a simple parabola could not account for the steep rise at longer wavelengths.

feature present in the template plus a global parabolic baseline so as to minimize the distance between the model and the data points. The number of free parameters is then eleven "line intensities" and three polynomial coefficients, for a total of 14 free parameters to be determined from 130 observed spectral points per line of sight. The main drawback of this method is that it does not allow for varying line widths or line centres; however, given the low resolution of ISOCAM's CVF this is not a serious drawback. We have found that integrated line emission estimated from methods 2 and 3 give results that agree to within 20 percent; numerical integration of Lorentzian line strengths, on the other hand, badly underestimates the energy carried in the extended line widths and hence this method has not been used.

References

Allain T., Leach S., Sedlmayr E., 1996, A&A 305, 602
Becklin E.E., Neugebauer G., Beckwith S., et al., 1976, ApJ 207, 770
Boulanger F., Boissel P., Cesarsky D., Ryter C., 1998, A&A 339, 194
Bradley J.P., Humecki H.J., Germani M.S., 1992, ApJ 394, 643
Bregman J.D., Allamandola L., Witteborn F.C., Tielens A.G.G.M., Geballe T.R., 1989, ApJ 344, 791
Cesarsky C.J., Abergel A, Agnèse P., et al. , 1996a, A&A 315, L32
Cesarsky D., Lequeux J., Abergel A., et al., 1996b, A&A 315, L309
Coulais A., Abergel A., 1998, In: Cox P., Kessler M. (eds.) The Universe as seen by ISO. ESA Special Publications series (SP-427), ESTEC, Noordwijk
Crovisier J., Leech K., Bockelee-Morvan D., et al., 1998, In: Cox P., Kessler M. (eds.) The Universe as seen by ISO. ESA Special Publications series (SP-427), ESTEC, Noordwijk
Dartois E., Cox P., Roelfsema P.R., et al. , 1998, A&A 338, L21
Demyk K., Jones A.P., Dartois E., et al. , 1999, A&A 349, 267
Désert F.X., Boulanger F., Léger A., et al. , 1986, A&A 159, 328
Désert F.X., Boulanger F., Puget J.L., 1990, A&A 237, 215
Draine B.T., Lee H.M., 1984, ApJ 285, 89
Draine B.T., 1985, ApJS 57, 587
Felli M., Churchwell E., Wilson T.L., Taylor G.B., 1993, A&AS 98, 137
Forrest W.J., Gillett F.C., Stein W.A., 1975, ApJ 195, 423
Gail H.-P., Sedlmayr E., 1999, A&A 347, 594
Gehrz R.D., Hackwell J.A., Smith J.R., 1975, ApJ 202, L33
Hallenbeck S.L., Nuth J.A., Daukantas P.L., 1998, Icarus 131, 198
Jaeger C., Molster F.J., Dorschner J., et al., 1998, A&A 339, 904
Jones A.P., Tielens A.G.G.M., Hollenbach D.J., 1996, ApJ 469, 740
Jones A.P., Frey V., Verstraete L., Cox P., Demyk K., 1998, In: Cox P., Kessler M. (eds.) The Universe as seen by ISO. ESA Special Publications series (SP-427), ESTEC, Noordwijk
Koike C., Shibai H., Tuchiyama A., 1993, MNRAS 264, 654
Malfait K., Waelkens C., Waters L.B.F.M., et al., 1998, A&A 332, L25
Marconi A., Testi L., Natta A., Walmsley C.M., 1998, A&A 330, 696
Ney E., Strecker D., Gehrz R., 1973, ApJ 180, 809
Pogge R.W., Owen J.M., Atwood B., 1992, ApJ 399, 147
Okumura K., 1999, The ISO point spread function and CAM beam profiles. Proceedings: ISO beyond point sources
Rouleau F., Martin P.G., 1991, ApJ 377, 526
Starck J.L., Abergel A., Aussel H., et al., 1998, A&AS 134, 135
Stein W.A., Gillett F.C., 1969, ApJ 155, L197
van Kerckhoven C., Hony S., Peters E., Tielens A.G.G.M., 2000, In: ISO beynd the peaks: The 2nd workshop on analytical spectroscopy. in press
van der Werf P., Stutzki J., Sternberg A., Krabbe A., 1996, A&A 313, 633
Verstraete L., Puget J.L., Falgarone E., et al., 1996, A&A 315, L337
Voors R.H.M., Waters L.B.F.M., Morris P.W., et al., 1998, A&A 341, L193
Waelkens C., Waters L.B.F.M., de Graauw M.S., et al. , 1996, A&A 315, L245
Waters L.B.F.M., Molster F.J., de Jong T., et al. , 1996, A&A 315, L361
Weaver W.B., Torres-Dodgen A.V., 1997, ApJ 487, 847